






 Cite this: *RSC Adv.*, 2019, 9, 12615

# Annealing atmosphere effect on the resistive switching and magnetic properties of spinel $\text{Co}_3\text{O}_4$ thin films prepared by a sol–gel technique

 Chuangye Yao,  Muhammad Ismail, Aize Hao,  Santhosh Kumar Thatikonda, Wenhua Huang, Ni Qin  and Dinghua Bao \*

Spinel  $\text{Co}_3\text{O}_4$  thin films were synthesized using a sol–gel technique to study the annealing atmosphere effect on resistive switching (RS) and magnetic modulation properties. Compared with oxygen and air annealed Pt/ $\text{Co}_3\text{O}_4$ /Pt stacks, the nitrogen annealed Pt/ $\text{Co}_3\text{O}_4$ /Pt stack shows optimal switching parameters such as a lower forming voltage, uniform distribution of switching voltages, excellent cycle-to-cycle endurance (>800 cycles), and good data retention. Improvement in switching parameters is ascribed to the formation of confined conducting filaments (CFs) which are composed of oxygen vacancies. From the analysis of current–voltage characteristics and their temperature dependence, the carrier transport mechanism in the high-field region of the high resistance state was dominated by Schottky emission. Besides, temperature dependent resistance and magnetization variations revealed that the physical mechanism of RS can be explained based on the formation and rupture of oxygen vacancy based CFs. In addition, multilevel saturation magnetization under different resistance states is attributed to the variation of oxygen vacancy concentration accompanied with the changes in the valence state of cations. Results suggested that using a nitrogen annealing atmosphere to anneal the thin films is a feasible approach to improve RS parameters and enhance the magnetic properties of  $\text{Co}_3\text{O}_4$  thin film, which shows promising applications to design multifunctional electro-magnetic coupling nonvolatile memory devices.

Received 13th February 2019

Accepted 17th April 2019

DOI: 10.1039/c9ra01121h

[rsc.li/rsc-advances](http://rsc.li/rsc-advances)

## 1. Introduction

Resistive random access memory (RRAM) devices, based on the resistive switching (RS) effect in a metal/insulator/metal (MIM) sandwiched structure, have become one of the most promising candidates for next-generation nonvolatile memories. Due to the simple MIM structure, RRAM devices have multiple advantages such as high storage density, fast switching speed, high scalability, low-energy consumption, and good compatibility with complementary metal oxide semiconductor (CMOS) technology.<sup>1–3</sup> The conversion of RRAM in its high-resistance state (HRS, or OFF) and low resistance state (LRS, or ON) can be accomplished by applying the voltage polarities.<sup>1</sup> The observed RS behaviors can be classified as bipolar, unipolar, complementary, and threshold switching.<sup>1,4,5</sup> In recent years, a variety of metal oxides such as RS active layers have been demonstrated to show the RS effect such as binary oxides  $\text{HfO}_2$ ,  $\text{ZnO}$ ,  $\text{Ta}_2\text{O}_5$ ,<sup>6–8</sup> ternary oxides  $\text{BiFeO}_3$ ,  $\text{CaTiO}_3$ , and ferrite materials,<sup>3,9,10</sup> along with complex oxides  $\text{Ba}_{0.6}\text{Sr}_{0.4}\text{TiO}_3$ ,  $\text{PrBa}_2\text{-Cu}_3\text{O}_x$ , and  $\text{La}_{0.3}\text{Pr}_{0.4}\text{Ca}_{0.3}\text{MnO}_3$ .<sup>11–13</sup>

However, until now, practical applications of RRAM are still under developed due to its controversial physical mechanism and the several reliability issues such as high electroforming voltage, uniformity of switching parameters, large fluctuation in HRS and LRS, deterioration of endurance and retention time. Intensive efforts have been devoted to overcome aforementioned challenges of RS parameters and to find out actual physical mechanism. For this purpose, many approaches, such as metal doping,<sup>14–17</sup> embedding metal nanoparticles,<sup>18,19</sup> bilayer structure,<sup>20–22</sup> as well as annealing atmosphere treatment,<sup>23–26</sup> have been adopted to minimize the challenges. Among them, annealing atmosphere treatment is not only good compatibility with CMOS process, but also a feasible and effective way to improve the performance and reliability of RRAM devices.<sup>27</sup> Also, some researchers have used annealing atmosphere to modulate oxygen vacancies in metal oxides,<sup>28</sup> because oxygen vacancies play an important role in RS effects of inert metal/oxide/inert metal sandwiched structure devices.<sup>11,14</sup> Sun *et al.* reported that hydrogen-annealed  $\text{ZnO}$  based RRAM device exhibited high  $R_{\text{on}}/R_{\text{off}}$  ratio and forming-free RS effect, which was ascribed to oxygen vacancy layer introduced at the top of  $\text{ZnO}$  interface.<sup>23</sup> Jin *et al.* also fabricated forming-free  $\text{Al/SnO}_x/\text{Pt}$  devices annealed in nitrogen, and explained forming-free switching due to sufficient oxygen vacancies generated in

State Key Laboratory of Optoelectronic Materials and Technologies, School of Materials Science and Engineering, Sun Yat-Sen University, Guangzhou 510275, China. E-mail: stsbdh@mail.sysu.edu.cn



the nitrogen-annealed  $\text{SnO}_x$  layer.<sup>29</sup> Rehman *et al.* introduced oxygen annealing in  $\text{Cu}_x\text{O}$  thin film based devices, and found that the  $R_{\text{on}}/R_{\text{off}}$  ratio increased about 3 orders of magnitude.<sup>24</sup> Above studies demonstrated that annealing atmosphere can significantly degrade or enhance the RS performance.<sup>24,29</sup> However, to date, the RS studies in annealing atmosphere are focused on only one gas atmosphere or single switching parameter.<sup>29</sup> Few reports are found in literature on systematical investigation into the effect of annealing atmosphere (oxygen, air, nitrogen) on the RS effect.

Compared with other RS materials, the superior RS properties in our previous work have been found in spinel-like  $\text{MgZnO}$  and spinel ferrite thin films (e.g.  $\text{NiFe}_2\text{O}_4$ ,  $\text{ZnFe}_2\text{O}_4$ ,  $\text{CoFe}_2\text{O}_4$ ),<sup>3,30–32</sup> which demonstrated that spinel structure materials exhibited excellent potential application in RS memories. Over the past decades, a lot of studies were exerted to magnetic oxides with spinel structure.<sup>33</sup> Moreover, binary spinel  $\text{Co}_3\text{O}_4$  also exhibited excellent RS performance and provided an opportunity in RS application owing to its simple binary component, facile synthetic technology, high chemical and thermal stabilities.<sup>34,35</sup> As an important role of binary metal oxide family,  $\text{Co}_3\text{O}_4$  is an outstanding candidate in optical-sensing, gas-sensing, electrical-sensing and magnetic-sensing devices, which have been widely used in photocatalysts, gas sensors, alkali-ion batteries, super-capacitors, electrocatalysis and magnetic devices.<sup>36–44</sup> So,  $\text{Co}_3\text{O}_4$  material provides a new approach in multifunctional device integration, such as optoelectronic and electro-magnetic devices. More importantly, the combination of both RS and magnetization modulated by electrical means has been one of the crucial issues to be studied for their promising applications in the next-generation information storage, such as memory with electrical writing and magnetic read operation, multilevel storage to obtain four logic states, and multifunctional electro-magnetic integrated devices.<sup>14,17,45–48</sup> Also, atmospheric thermal annealing was an effective cost-efficiently approach for magnetism applications. Li *et al.* introduced atmospheric thermal annealing to BN-nanoplate based spintronic nanodevice research, revealing defect-induced ferrimagnetism.<sup>49</sup> Gao *et al.* investigated annealing atmosphere effect on Mn-doped  $\text{ZnO}$  samples, and found room temperature ferromagnetism in  $\text{H}_2$ -annealed sample.<sup>50</sup> Li *et al.* adopted  $\text{H}_2$  atmospheric annealing to precisely perform control of  $\text{Cr}_{0.046}\text{Zn}_{0.954}\text{O}$ ,<sup>51</sup> and also controlled a specific  $\text{CO}_2/\text{CO}$  atmosphere ratio to research magnetoresistance behavior of magnetic magnetite.<sup>52</sup> Besides, RS control of magnetization is compatible with CMOS technology,<sup>45,47</sup> which motivates us to explore how to improve RS performance and induce magnetization variations of  $\text{Co}_3\text{O}_4$  thin films by different annealing atmosphere. However, the study of RS properties on  $\text{Co}_3\text{O}_4$  materials is quite limited and to the best of our knowledge, annealing atmosphere effect has not yet been reported.

In this work, we have synthesized spinel  $\text{Co}_3\text{O}_4$  thin films by sol-gel process to study the different annealing atmospheres effect on RS and magnetic properties. Lower forming voltage, uniform distribution of switching voltages, excellent cycle-to-cycle endurance (>800 cycles), and good data retention ( $10^4$  s)

were obtained in nitrogen annealed  $\text{Pt}/\text{Co}_3\text{O}_4/\text{Pt}$  stack. Temperature dependence of resistances at HRS and LRS and magnetic modulation give a clue to explain the physical mechanisms of RS and associated magnetization variations.

## 2. Experimental procedure

The  $\text{Co}_3\text{O}_4$  thin films were prepared by a sol-gel deposition method. The  $\text{Co}(\text{CH}_3\text{COO})_3 \cdot 4\text{H}_2\text{O}$  was dissolved in 2-methoxyethanol and acetic acid to form  $0.1 \text{ mol L}^{-1}$   $\text{Co}_3\text{O}_4$  precursor solution with 2-methoxyethanol and acetic acid of volume ratio 2 : 1. Prepared precursor solution was spin-coated on the  $\text{Pt}/\text{Ti}/\text{SiO}_2/\text{Si}$  substrates at a speed of 3000 rpm for 30 s, and consequently the films were baked at  $300^\circ\text{C}$  for 5 min. The above spin coating and baking treatment procedures were repeated several times until the desired films were obtained. After that, the  $\text{Co}_3\text{O}_4$  thin films on  $\text{Pt}/\text{Ti}/\text{SiO}_2/\text{Si}$  substrates were annealed in oxygen, air, and nitrogen atmosphere at  $600^\circ\text{C}$  for 1 h. Then, to define the cell size of the MIM structure,  $300 \mu\text{m}$  metal shadow mask were used. Finally, Pt top electrode (TE) was deposited on the surface of  $\text{Co}_3\text{O}_4$  films to form the  $\text{Pt}/\text{Co}_3\text{O}_4/\text{Pt}$  stack.

Crystal structures of  $\text{Co}_3\text{O}_4/\text{Pt}$  substrates with different annealing atmospheres were characterized by X-ray diffractometer (XRD, Rigaku D/MAX 2200 VPC) with  $\text{Cu K}\alpha$  radiation. In addition, surface morphologies, film thickness and cross-sectional view of  $\text{Pt}/\text{Co}_3\text{O}_4/\text{Pt}$  stacks were analyzed by scanning electron microscopy (SEM, Gemini 500). Furthermore, chemical states of  $\text{Co}_3\text{O}_4$  films were examined by X-ray photoelectron spectroscopy (XPS, ESCALAB 250). The measurements of current-voltage ( $I$ - $V$ ) characteristics were performed using a Keithley 236 sourcemeter in direct current (DC) sweep mode under air ambient at room temperature. Temperature dependent resistances of HRS and LRS were also measured in the range of 200 to 300 K. Magnetic properties of  $\text{Pt}/\text{Co}_3\text{O}_4/\text{Pt}$  stack were characterized by a superconducting quantum interference device (SQUID) magnetometer (Quantum Design). The applied magnetic field was in the range from  $-2$  to  $+2$  tesla at room temperature, and  $\text{Pt}/\text{Co}_3\text{O}_4/\text{Pt}$  stack was placed parallel (in-plane) or perpendicular to the applied magnetic field.

## 3. Results and discussion

Fig. 1 shows the XRD patterns of  $\text{Co}_3\text{O}_4/\text{Pt}$  substrate annealed in oxygen, air, and nitrogen atmosphere at  $600^\circ\text{C}$  for 1 h. It can be seen that all the peaks of  $\text{Co}_3\text{O}_4$  films are well matched with JCPDS data (card no. 74-2120), except for  $\text{Pt}/\text{Ti}/\text{SiO}_2/\text{Si}$  substrate.<sup>53</sup> There is no evidence of any other impurity peaks from Co and  $\text{CoO}$ , indicating the pure crystallization of the  $\text{Co}_3\text{O}_4$  films. In addition, compared with nitrogen annealed  $\text{Co}_3\text{O}_4$  film, oxygen and air annealed  $\text{Co}_3\text{O}_4$  films show higher peak intensity and narrower full width at half maximum (FWHM). It means that nitrogen annealing atmosphere reduces the crystallinity of  $\text{Co}_3\text{O}_4$  film, which is highly suitable for the improvement of RS parameters. Usually, the average grain size ( $D$ ) of the  $\text{Co}_3\text{O}_4$  thin films can be calculated using the Scherrer formula:<sup>54</sup>



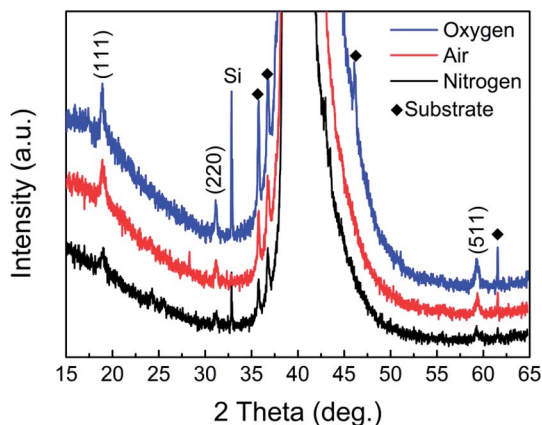


Fig. 1 X-ray diffraction patterns of  $\text{Co}_3\text{O}_4$  thin films annealed in oxygen, air, and nitrogen.

$$D = 0.9\lambda/\beta \cos \theta \quad (1)$$

where  $\lambda = 0.154056$  nm is the X-ray wavelength of  $\text{Cu } \alpha$  irradiation,  $\beta$  is the full width at half maximum, and  $\theta$  is the Bragg diffraction angle. By calculating the average value of grain size from the (111), (220), and (511) diffraction peaks. The average crystallite sizes are estimated to be  $\sim 22.1$ ,  $\sim 17.5$ , and  $\sim 9.8$  nm for the annealed  $\text{Co}_3\text{O}_4$  thin films in oxygen, air, and nitrogen atmosphere, respectively.

SEM analysis was carried out to study the surface morphologies of  $\text{Co}_3\text{O}_4$  films on  $\text{Pt}/\text{Ti}/\text{SiO}_2/\text{Si}$  substrates as shown in Fig. 2(a–c). The results show that annealing atmosphere has great effects on surface morphology of the  $\text{Co}_3\text{O}_4$  films. In addition, SEM analysis illustrates that  $\text{Co}_3\text{O}_4$  films are smooth, uniform, and crack-free for surface morphology. Meanwhile, the grain size of  $\text{Co}_3\text{O}_4$  films annealed at oxygen atmosphere is larger as that of nitrogen annealed  $\text{Co}_3\text{O}_4$  films, which is in good agreement with XRD results. The above results also demonstrate that annealing atmosphere can directly affect the crystal growth, grain boundary amount, and grain size of the  $\text{Co}_3\text{O}_4$  films, which may play an important role in their electrical properties. Fig. 2(a1–c1) show the particle size distributions of  $\text{Co}_3\text{O}_4$  films annealed in oxygen, air and nitrogen atmosphere, respectively. The particle size was obtained in terms of the log-normal distribution fitting.<sup>55</sup> From the histogram, the average particle sizes of oxygen, air, and nitrogen annealed  $\text{Co}_3\text{O}_4$  films are found to be  $\sim 20$ ,  $\sim 15$ , and  $\sim 8$  nm, respectively. Based on the average particle size evaluation, it can be seen that nitrogen annealed stack have minimum particles size which is optimum particle size to improve the switching parameters of the RRAM stacks. These particles are nanocrystalline in nature, revealing good agreement with calculated XRD results.

XPS analysis was utilized to evaluate the concentration of oxygen vacancies or defect in the  $\text{Co}_3\text{O}_4$  films annealed in oxygen, air, and nitrogen atmosphere, respectively. Fig. 3 shows the curve fitting results of O 1s spectra of  $\text{Co}_3\text{O}_4$  films annealed at oxygen, air and nitrogen atmosphere. The peaks can be fitted by three peaks centered at 530.1, 531.6, and 533.2 eV, namely  $\text{O}_\text{L}$ ,  $\text{O}_\text{V}$ ,  $\text{O}_\text{C}$ , respectively, which corresponds to lattice oxygen,

oxygen vacancies, and chemisorbed oxygen in deficient regions, respectively.<sup>53,56,57</sup> The result shows that the amounts of oxygen vacancies are 21.1%, 30.3%, and 32.1% in oxygen-annealing, air-annealing, and nitrogen-annealing  $\text{Co}_3\text{O}_4$  films, respectively. These results revealed that oxygen vacancies concentration or area of defect is higher in nitrogen annealed  $\text{Co}_3\text{O}_4$  films as compared to oxygen and air annealed stacks. The nitrogen annealed  $\text{Co}_3\text{O}_4$  films reduce the crystallinity and bring numerous grain boundaries, and generate the loss of oxygen atoms in the surface of  $\text{Co}_3\text{O}_4$  and thus introduce oxygen vacancies.<sup>53,57</sup> XPS results are in good agreement with XRD and SEM analysis.

Annealing atmosphere dependence of RS characteristics was investigated. All measured memory cells showed high resistance state (HRS) for the first time, and transformed from HRS to low resistance state (LRS) by increasing the voltage sweep at certain level of current to initiate RS behavior, which is usually called “forming”. During the forming process, it is necessary for all memory cells to set the compliance current of 10 mA to prevent permanent hard breakdown. Fig. 4(a) illustrates the variations of forming voltages with annealing in oxygen, air, and nitrogen atmosphere. It can be seen that all the  $\text{Pt}/\text{Co}_3\text{O}_4/\text{Pt}$  stacks exhibited lower forming voltage in the range between 2 to 6 V, respectively. Compared with oxygen annealed and air annealed  $\text{Pt}/\text{Co}_3\text{O}_4/\text{Pt}$  stacks, stack annealed in nitrogen atmosphere obtained smaller forming voltage due to introducing more defects such as oxygen vacancies during annealing. After the forming process, a reset process begins from 0 to negative 1.5 V without limiting the current level, all stack switches back to HRS (lower than the initial resistance). All the memory cells were set in the positive voltage region and reset in negative voltage region, as shown in Fig. 4(b–d). All the measured cells show typical bipolar RS behaviors.

Endurance characteristic is one of the essential parameters of RRAM memory stacks. Fig. 5(a–c) shows the DC endurance characteristics of all memory stacks measured at a read voltage of 0.1 V. The nitrogen annealed  $\text{Pt}/\text{Co}_3\text{O}_4/\text{Pt}$  stack displayed relatively low  $R_{\text{on}}/R_{\text{off}}$  ratio and small fluctuation in HRS and LRS, which is caused by better conductivity of  $\text{Co}_3\text{O}_4$  film with Pt electrode. It means that more defects such as oxygen vacancies are generated during nitrogen annealing. Reduction of HRS of nitrogen annealed  $\text{Co}_3\text{O}_4$  films is due to lower crystallinity as compared to other annealed stacks, which leads to create more defects or oxygen vacancies at the grain boundaries. Hao *et al.* reported that low crystallinity can induce rich oxygen vacancies in  $\text{Co}_3\text{O}_4$ , because numerous lattice boundaries were caused by the poor crystallinity and contributed to the generation of oxygen vacancies, resulting in improved conductivity.<sup>57</sup> In addition, improvement in fluctuation of HRS and LRS is due to more oxygen vacancies reserved in the grain boundaries.<sup>3,11,57</sup> Enough number of oxygen vacancies form the confine CFs along with grain boundaries,<sup>11</sup> acting as modulation in the growth of CFs (shape and location), which caused that the larger possibility of formation and rupture of filaments occurred in the same location and resulted in more stable endurance characteristics. It is worth mentioning that four times repeatable number of cycles increased in nitrogen annealed  $\text{Pt}/\text{Co}_3\text{O}_4/\text{Pt}$





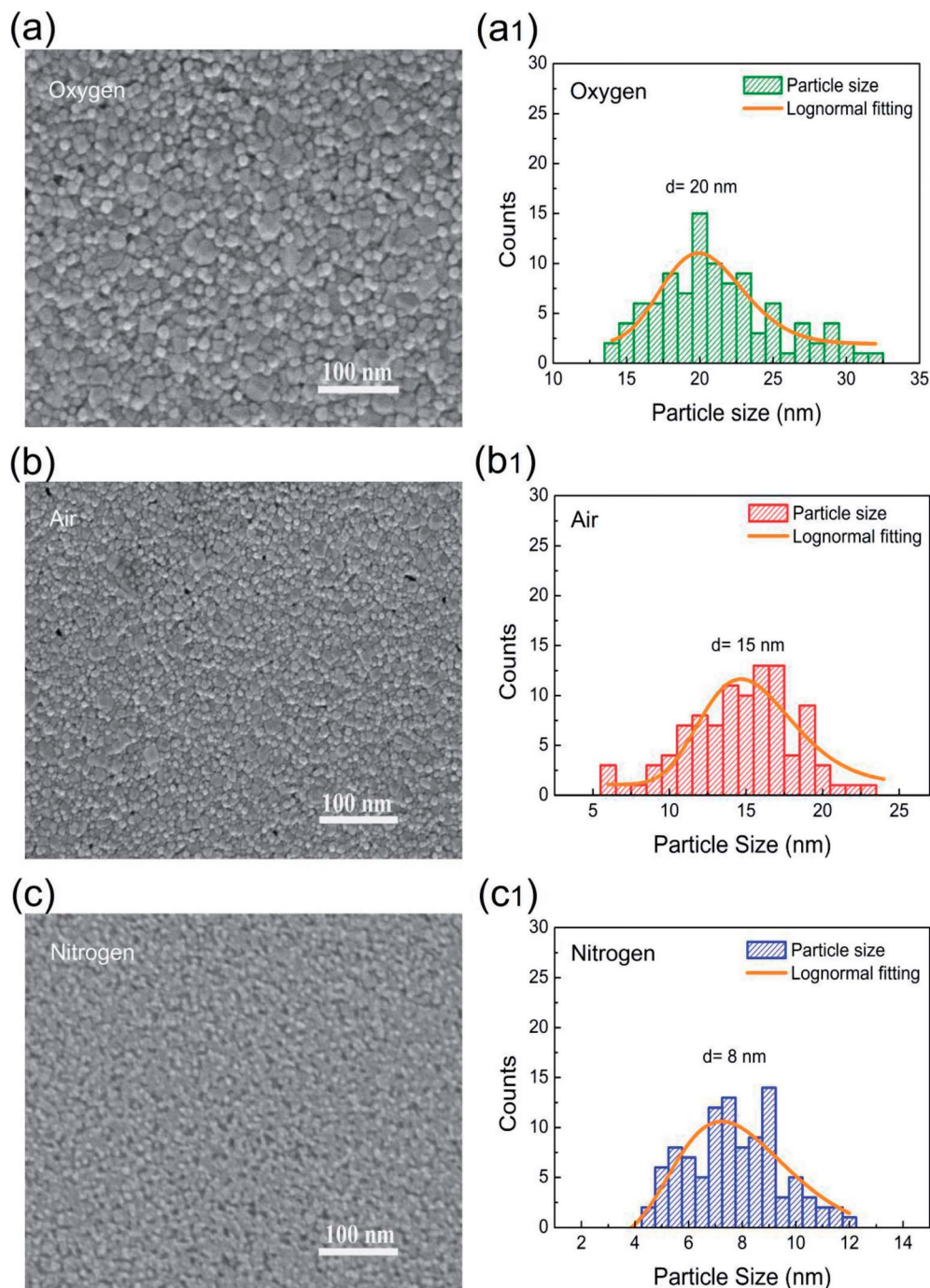


Fig. 2 The surface morphology images of  $\text{Co}_3\text{O}_4$  thin films annealed in (a) oxygen, (b) air, and (c) nitrogen atmosphere, respectively. Corresponding statistical distributions of particle sizes of  $\text{Co}_3\text{O}_4$  thin films with annealing in (a1) oxygen, (b1) air, and (c1) nitrogen atmosphere.

stack as compared to other air and oxygen annealed Pt/ $\text{Co}_3\text{O}_4$ /Pt stacks.

To further evaluate the switching uniformity of different atmosphere annealed Pt/ $\text{Co}_3\text{O}_4$ /Pt stacks, cumulative probability distribution of the set and reset voltages is shown in Fig. 6(a). Relatively much smaller fluctuation is noted in set and reset voltage of nitrogen annealed Pt/ $\text{Co}_3\text{O}_4$ /Pt stack, indicating to their better uniformity in the RS characteristics as compared to other oxygen and air annealed Pt/ $\text{Co}_3\text{O}_4$ /Pt stacks. The oxygen

annealed Pt/ $\text{Co}_3\text{O}_4$ /Pt stack exhibit larger variation in  $V_{\text{set}}$  (+0.6 V to +2.3 V) and  $V_{\text{reset}}$  (−0.4 to −0.86 V). Also, for air annealed Pt/ $\text{Co}_3\text{O}_4$ /Pt stack, the set voltage ranges from +0.75 to +1.35 V and reset voltages from −0.38 to −0.7 V, respectively. However, nitrogen annealed Pt/ $\text{Co}_3\text{O}_4$ /Pt stack reduced these voltage dispersions, that is,  $V_{\text{set}}$  (+0.75 to +1.1 V) and  $V_{\text{reset}}$  (−0.4 to −0.7 V) as shown in Fig. 6(a). Interestingly, nitrogen annealing can significantly improve uniformity in switching parameters. It is expected that nitrogen annealing probably



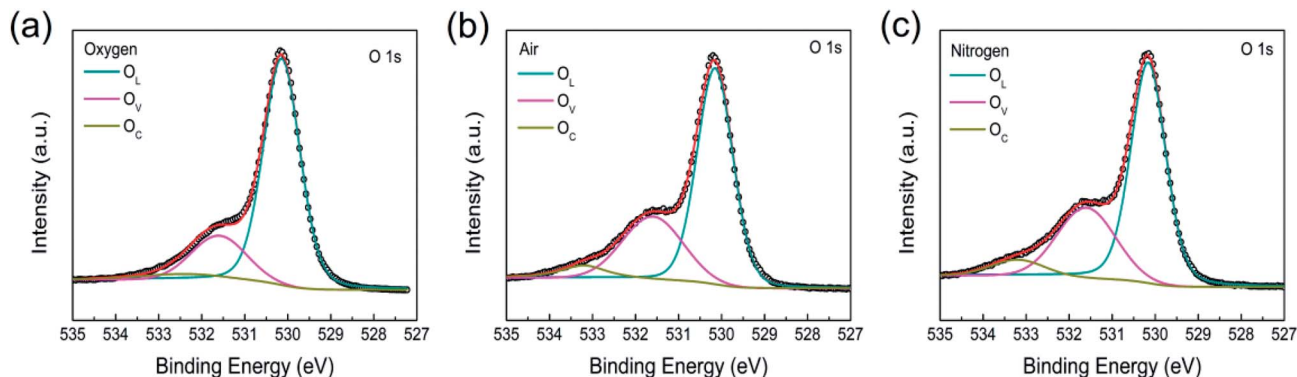


Fig. 3 XPS spectra of O 1s for (a) oxygen (b) air, and (c) nitrogen annealed  $\text{Co}_3\text{O}_4$  thin films.

enhances the strength of oxygen vacancies within the  $\text{Co}_3\text{O}_4$  matrix, which results in a reduction in set and reset voltages. Jin *et al.* also reported that uniformity of set and reset voltages was improved through nitrogen annealing as compared to other air annealed  $\text{SnO}_x$  based devices.<sup>29</sup> Finally, nitrogen annealed Pt/ $\text{Co}_3\text{O}_4$ /Pt stack is demonstrated superior performance in terms of excellent endurance properties and good cycle-to-cycle uniformity as compared to other stacks. Fig. 6(b) depicts the

retention characteristics of the nitrogen annealed Pt/ $\text{Co}_3\text{O}_4$ /Pt stack. Retention measurement was performed at room temperature with a read voltage of 0.1 V. It is noted that both HRS and LRS are stable up to  $10^4$  s. The stability on both HRS and LRS confirms perfection for nonvolatile memory data storage applications.

Fig. 7 illustrates the carrier transport conduction mechanism of the nitrogen annealed Pt/ $\text{Co}_3\text{O}_4$ /Pt stack. Fig. 7(a)

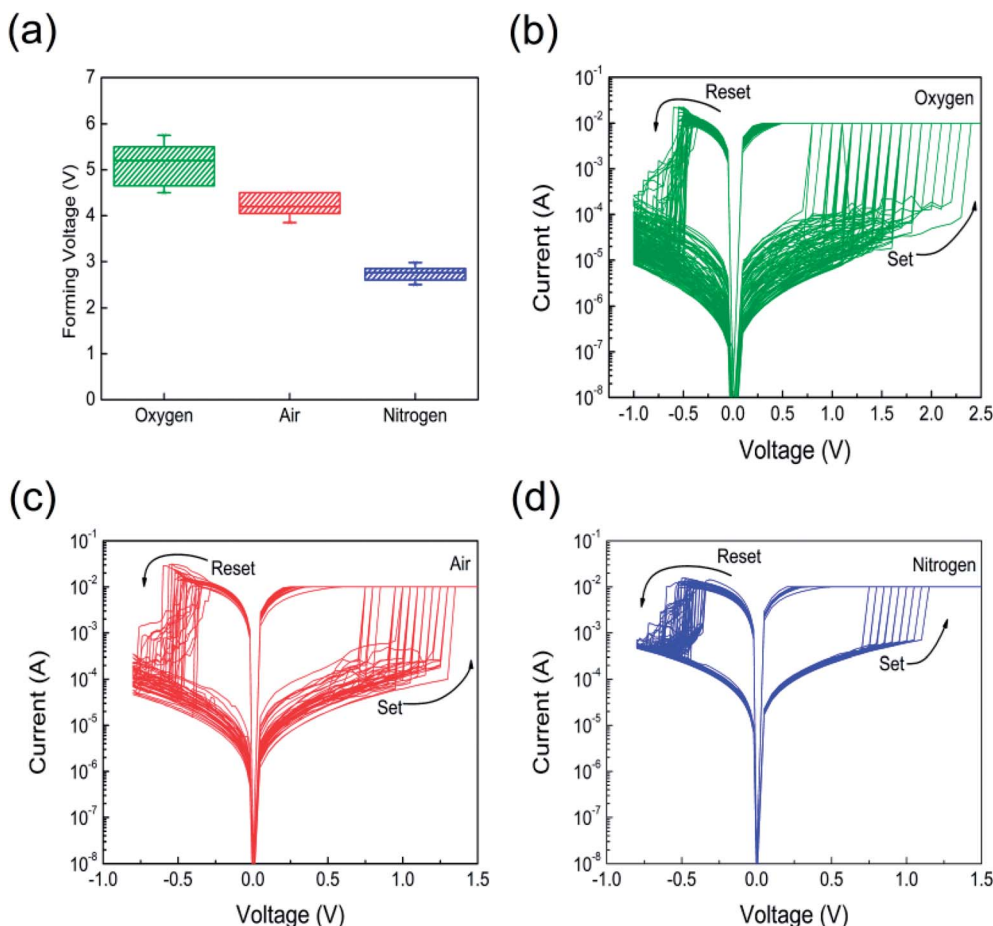


Fig. 4 (a) Variations of electroforming voltages with different annealing atmosphere. Typical  $I$ - $V$  curves after the electroforming process in different annealing atmosphere: (b) oxygen, (c) air, and (d) nitrogen.



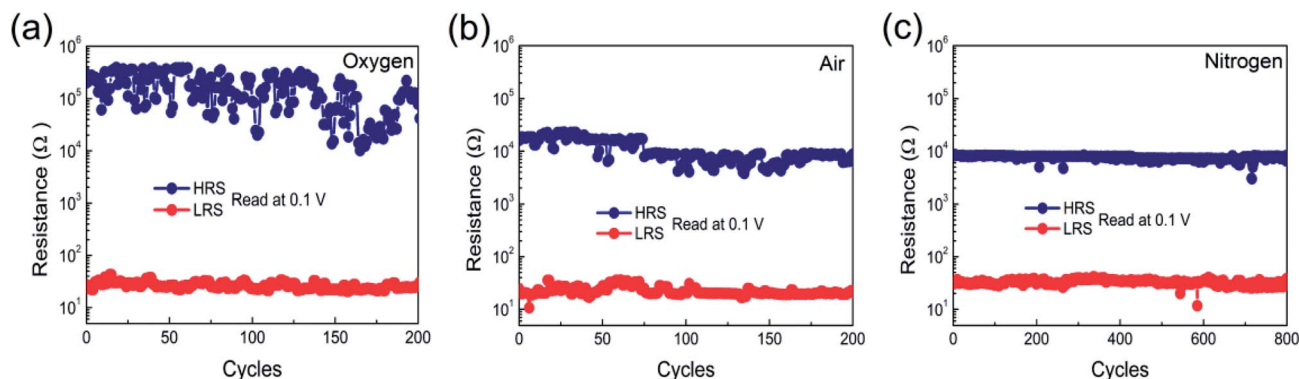


Fig. 5 Endurance performance of  $\text{Co}_3\text{O}_4$  thin films in different annealing atmosphere: (a) oxygen, (b) air, and (c) nitrogen.

depicts the double-log scale plots of  $I$ - $V$  curves fitting at LRS. In the LRS, the conduction mechanism is ohmic behavior as demonstrated by the linear slope of  $\sim 1.04$ , suggesting filaments growth and connection between top and bottom electrode. In the low voltage region of HRS, the carrier transport also obeyed ohmic conduction behavior because thermally generated free carrier concentrations are higher than the injected carriers.<sup>17,32,34</sup> In the higher voltage region of HRS, the  $I$ - $V$  curves were fitted with different carrier transport mechanism such as Schottky emission, Poole-Frenkel emission, and space charge limited current (SCLC), respectively. We found linear curve fitting with Schottky emission,<sup>17</sup> as shown in Fig. 7(b). The linear relation of  $\ln(I)$  vs.  $\text{Sqrt}(V)$  indicates that electrons achieve an adequate energy to conquer the energy barrier. Schottky emission mechanism can be expressed by the following equation:<sup>17</sup>

$$J = A^* T^2 \exp \left[ -q \left( \Phi_B - \sqrt{qE/4\pi\epsilon} \right) / kT \right] \quad (2)$$

where  $J$  is the current density,  $A^*$  is the effective Richardson constant,  $T$  is the temperature,  $q$  is the electron charge,  $\Phi_B$  is the effective Schottky barrier height,  $E$  is the electric field, and  $\epsilon$  is the dielectric constant, and  $k_B$  is a Boltzmann's constant, respectively.

Temperature dependence of  $I$ - $V$  characteristics is one of the best tools to further confirm whether Schottky emission mechanism is dominated in higher voltage region of HRS. The  $I$ - $V$  characteristics were measured in the range of 200 to 300 K. Fig. 8(a) shows the temperature dependence of the high and low resistance states of nitrogen annealed Pt/ $\text{Co}_3\text{O}_4$ /Pt stack. The resistance value of HRS decreases with increasing temperature, which indicates a semiconducting behavior. Furthermore, the temperature dependent  $I$ - $V$  curves measured at the voltage range from 0.4 to 0.6 V were plotted as  $\ln(I/T^2)$  vs.  $1/T$  in HRS of nitrogen annealed Pt/ $\text{Co}_3\text{O}_4$ /Pt stack, as shown in Fig. 8(b), which confirmed the linear fitting with Schottky emission.<sup>17</sup> In contrast, the resistance value of LRS increases with increasing temperature, indicating a metallic conducting behavior. Fig. 8(c) shows the linear fitting of the resistance value of LRS according to the equation  $R(T) = R_0(1 + \alpha(T - T_0))$ . The resistance temperature coefficient  $\alpha$  is measured to be  $7.8 \times 10^{-4} \text{ K}^{-1}$ , and similar results were also reported in our previous Pt/NiFe<sub>2</sub>O<sub>4</sub>/Pt based memory devices,<sup>3</sup> which indicated that the CFs are composed of oxygen vacancies.

The magnetic characteristics associated with RS could play a crucial role in exploring multifunctional device design of spinel  $\text{Co}_3\text{O}_4$  films. Fig. 9 displays the magnetization-magnetic

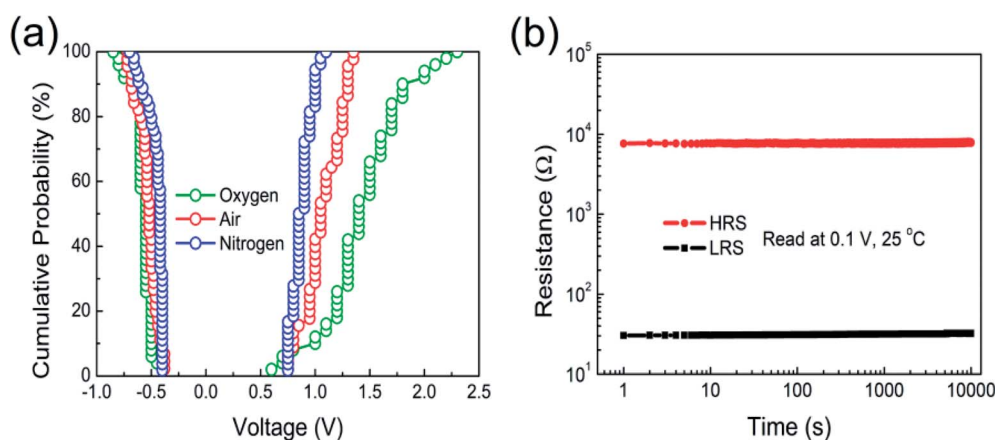


Fig. 6 (a) Statistical distribution of the set and reset voltages of  $\text{Co}_3\text{O}_4$  thin films in different annealing atmosphere. (b) Retention capability of Pt/ $\text{Co}_3\text{O}_4$ /Pt device annealed in nitrogen.



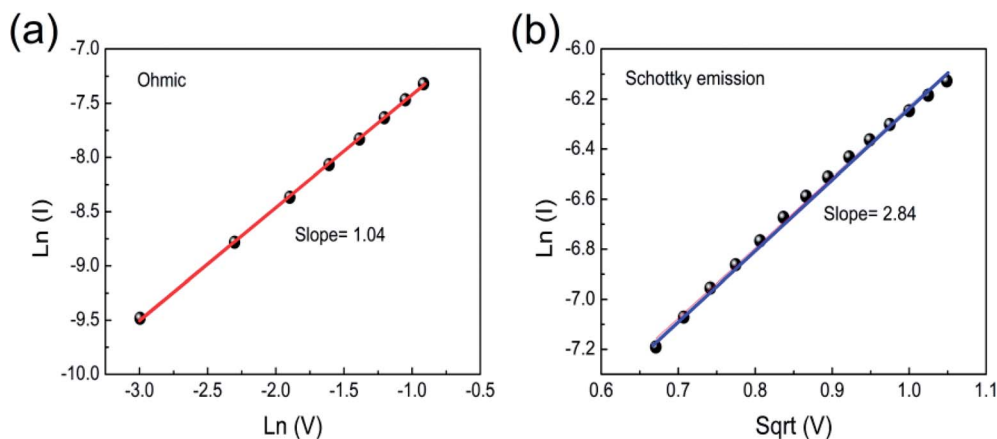


Fig. 7 (a) The double-log scale plots of  $I$ - $V$  curves at LRS. (b) The  $I$ - $V$  curves fitted with  $\ln(I)$  versus  $\text{Sqrt}(V)$  plot at HRS for  $\text{Co}_3\text{O}_4$  thin film in nitrogen annealing atmosphere.

field ( $M$ - $H$ ) hysteresis loops of  $\text{Co}_3\text{O}_4$  thin films with different annealing atmosphere at room temperature, showing all  $\text{Co}_3\text{O}_4$  films have a ferromagnetic behavior. Fig. 9(a-c) show in-plane  $M$ - $H$  loops of  $\text{Co}_3\text{O}_4$  films annealed in oxygen, air, and nitrogen atmosphere, respectively. It is found that the values of saturation magnetization in fresh or initial state for  $\text{Co}_3\text{O}_4$  films annealed in oxygen, air, and nitrogen are consecutively increased due to decrease of grain sizes confirmed by XRD and SEM results, in good agreement with the existed report.<sup>58</sup> It is further observed that  $\text{Co}_3\text{O}_4$  films annealed in same atmosphere exhibit multilevel saturation magnetization with the change of resistance states. All the saturation magnetization ( $M_s$ ) relationship of  $\text{Pt}/\text{Co}_3\text{O}_4/\text{Pt}$  stacks exhibits  $M_{s(\text{LRS})} > M_{s(\text{HRS})} > M_{s(\text{fresh})}$ . Compared with the  $M$ - $H$  loops of  $\text{Co}_3\text{O}_4$  films annealed in oxygen or air atmosphere, the values of saturation magnetization in nitrogen annealed  $\text{Co}_3\text{O}_4$  thin films, regardless of fresh state, HRS, and LRS, correspondingly increase, which indicates the enhanced ferromagnetic behavior. The saturation magnetization of nitrogen annealed  $\text{Pt}/\text{Co}_3\text{O}_4/\text{Pt}$  stack indicates remarkable variations at different resistance states, and the value of saturation magnetization for fresh state, HRS, and LRS are 50.4, 89.2, and 140.5  $\text{emu cm}^{-3}$ , respectively, in which the saturation magnetization changes are about 64%.

The remarkable multilevel saturation magnetization can provide an opportunity to design multi-state electric and magnetic integrated stacks.<sup>14,17</sup> The variation in saturation magnetization with different resistance states could be ascribed to variation in oxygen vacancy concentration as well as associated contributions originated from changes in valence states of  $\text{Co}^{3+}$  and  $\text{Co}^{2+}$  ions. Previous studies also demonstrated that the variation in oxygen vacancy concentration caused changes in magnetization.<sup>59,60</sup> Fig. 9(d-f) shows the perpendicular plane  $M$ - $H$  loops, which demonstrates that the magnetization is anisotropic compared with in-plane  $M$ - $H$  loops, being lower when the magnetic field is applied perpendicularly to the surface of  $\text{Co}_3\text{O}_4$  thin film than when it is applied in the parallel direction.

Based on the experimental results and discussion above, the model on the basis of formation and rupture of oxygen vacancies based CFs is depicted to explain the physical mechanism of RS and magnetization modulation behaviors, as shown in Fig. 10. It is worth mentioning here that bulk  $\text{Co}_3\text{O}_4$  materials have a normal spinel structure with the cobalt ions in the form of  $\text{Co}^{2+}$  and  $\text{Co}^{3+}$  oxidation states occupying interstitial tetrahedral ( $T_d$ ) and octahedral ( $O_h$ ) sites, respectively.<sup>61</sup> The  $\text{Co}^{3+}$  ions at  $O_h$  sites exhibit no magnetic moment due to the large

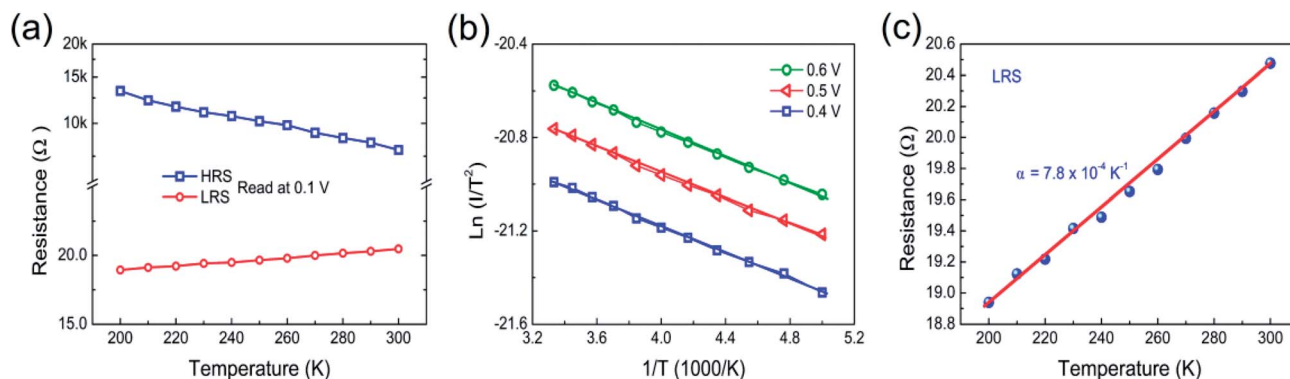


Fig. 8 (a) The temperature dependence of  $\text{Pt}/\text{Co}_3\text{O}_4/\text{Pt}$  device annealed in nitrogen at HRS and LRS. (b)  $\ln(I/T^2)$  versus  $1/T$  at higher-voltage region of HRS of  $\text{Pt}/\text{Co}_3\text{O}_4/\text{Pt}$  device. (c) The resistance temperature coefficient fitting at LRS from 200 K to 300 K.





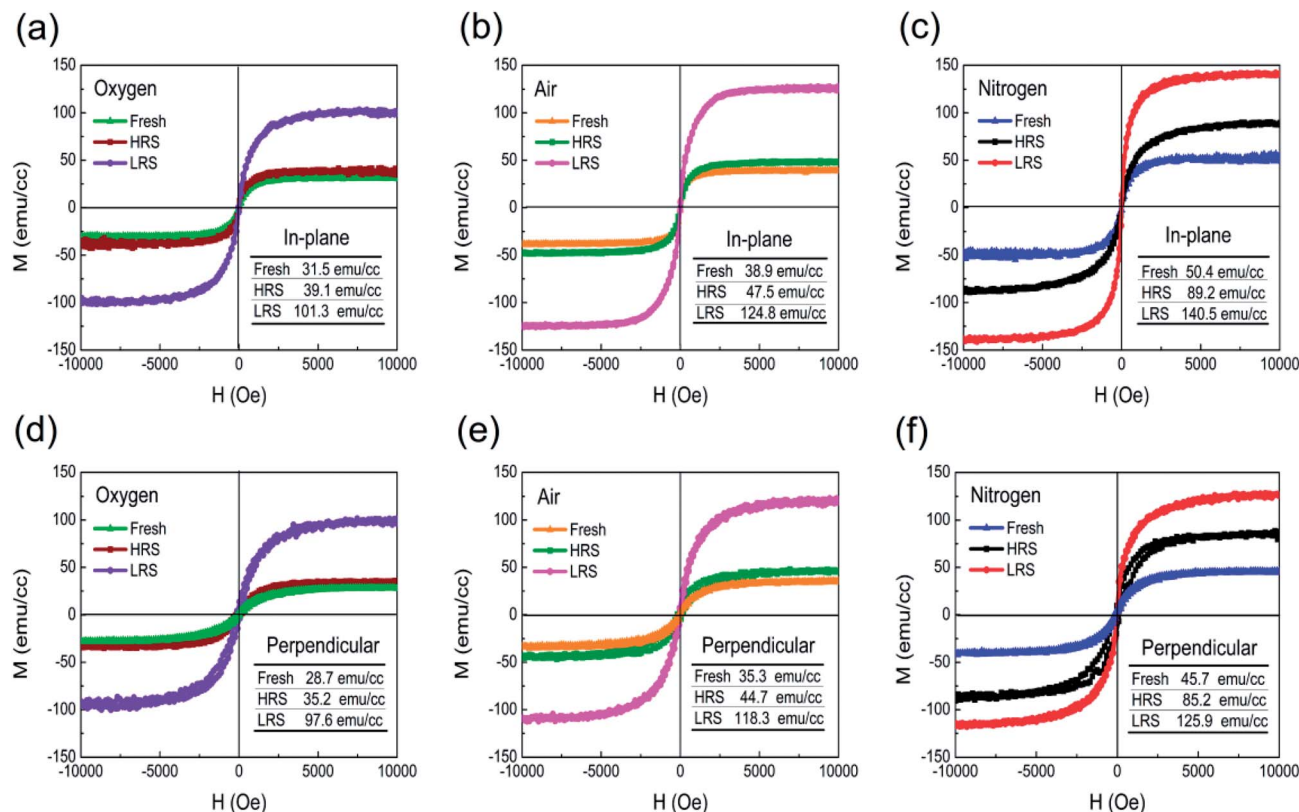


Fig. 9 (a–c) In-plane, and (d–f) perpendicular plane M–H loops of Pt/Co<sub>3</sub>O<sub>4</sub>/Pt stacks with various resistance states annealed in oxygen, air, and nitrogen atmosphere, respectively.

splitting of the 3d orbital in symmetry structure and Co<sup>2+</sup> ions at T<sub>d</sub> sites hold a magnetic moment.<sup>44,61</sup> Usually, bulk Co<sub>3</sub>O<sub>4</sub> shows antiferromagnetic behavior, which is dominated by the T<sub>d</sub>–T<sub>d</sub> weak antiferromagnetic interaction.<sup>44,62,63</sup> Studies show that nonmagnetic oxides can exhibit ferromagnetic behavior in the form of thin films, which originates from the changes of oxygen vacancy concentration, and accords with our prepared Co<sub>3</sub>O<sub>4</sub> films as shown in Fig. 9.<sup>59,60,64</sup> Usually, the oxygen vacancies can inevitably be introduced in Co<sub>3</sub>O<sub>4</sub> thin film during deposition process.<sup>65</sup> The magnetism of thin films increases by increasing the oxygen vacancy concentration.<sup>60</sup> Also, the ferromagnetic characteristics of films can be created by cation disordering such as partial Co<sup>2+</sup> ions occupying the O<sub>h</sub> sites and displacement of some Co<sup>3+</sup> from the O<sub>h</sub> positions to the T<sub>d</sub> positions, and similar cases occurred in the Mn<sub>3</sub>O<sub>4</sub> and ZnFe<sub>2</sub>O<sub>4</sub> thin films.<sup>60</sup> Thus, the super-exchange interactions between Co<sup>2+</sup> at T<sub>d</sub> and O<sub>h</sub> positions change the magnetic coupling of Co<sup>2+</sup>(T<sub>d</sub>)–Co<sup>2+</sup>(T<sub>d</sub>) from antiferromagnetic to ferromagnetic characteristics.<sup>44</sup> However, after electroforming process, a large number of oxygen vacancies can easily be induced by electrical impulse,<sup>3</sup> which results in lower saturation magnetization at fresh state than at HRS and LRS of Pt/Co<sub>3</sub>O<sub>4</sub>/Pt stack in Fig. 9. That is why the oxygen vacancies based CFs mechanism is responsible for the RS characteristics of the inert electrode/oxide/inert electrode sandwiched structure.<sup>14</sup> When the sandwiched structure is activated by a set voltage, the resistance of the Pt/Co<sub>3</sub>O<sub>4</sub>/Pt devices would switch from HRS to

LRS. At the same time, oxygen ions are much more mobile than the cobalt cations and its migration jumps from the oxygen coordination in the lattice, which results in generation and accumulation of multiple oxygen vacancies.<sup>60,66</sup> Then, the oxygen vacancies based CFs are connected between the top electrode and bottom electrode. On increasing oxygen vacancy concentration, the Co<sup>3+</sup> ions occupying the O<sub>h</sub> positions are converted into Co<sup>2+</sup> ions, and the super-exchange interactions of Co<sup>2+</sup>(T<sub>d</sub>)–Co<sup>2+</sup>(T<sub>d</sub>) are also enhanced, which results in the enhancement of saturation magnetization.<sup>44</sup> In contrast, when the sandwiched structure is activated by a reset voltage, the resistance of the Pt/Co<sub>3</sub>O<sub>4</sub>/Pt devices would switch from LRS to HRS. At the same time, the oxygen vacancies based CFs are ruptured by the high current-induced Joule heating effect during the reset process.<sup>34,67</sup> Also, the oxygen ions migrate backwards and recombine with the oxygen vacancies, which results in decrease of the oxygen vacancy concentration. Therefore, the decrease of the super-exchange interaction of Co<sup>2+</sup>(T<sub>d</sub>)–Co<sup>2+</sup>(T<sub>d</sub>) as the decrease of numbers of oxygen vacancies, which can accompany by the reductions in the saturation magnetization. That is, the resistive switching properties are ascribed to the formation and rupture of oxygen vacancies based CFs accompanying with changes in the valences of cations (Co<sup>2+</sup> and Co<sup>3+</sup>) due to the redox effect.

In forming or set process, connecting the top and bottom electrodes with the help of oxygen vacancies based CFs *via* external electric bias, resulted in that stacks switched to LRS, as





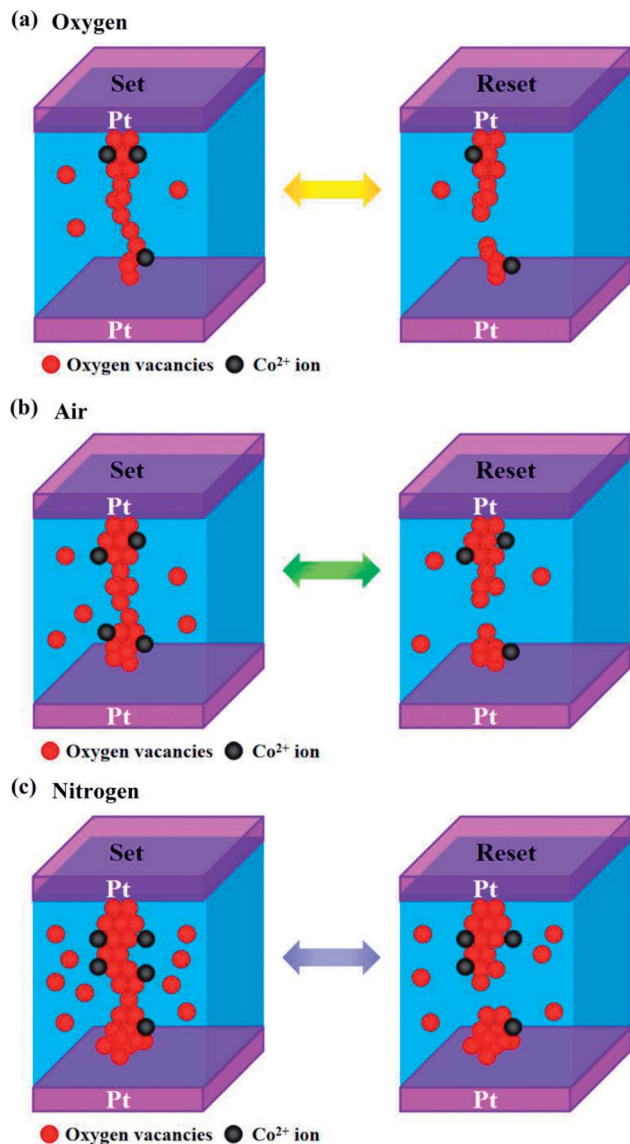


Fig. 10 Schematic representation of switching mechanism. Formation of conducting filament at the set process and rupture of conducting filament at the reset process in different annealing atmosphere: (a) oxygen, (b) air, and (c) nitrogen.

shown in Fig. 10. In the reset process, high current induced Joule heating effect to rupture the CFs in  $\text{Co}_3\text{O}_4$  thin films, accompanying with stack switching from LRS to HRS.<sup>34</sup> Fig. 10(a) and (b) show the schematic diagram of oxygen and air annealed  $\text{Pt}/\text{Co}_3\text{O}_4/\text{Pt}$  stacks, respectively. The oxygen vacancies content was lower in oxygen annealed stack as compared to air annealed stack. Less concentration of oxygen vacancies in oxygen annealed stack caused higher forming voltage and instability switching parameters. On the other side, air annealed stack has comparatively higher concentration of oxygen vacancies. That's why in nitrogen annealed stack, reduction of forming voltage and suppression of random CFs growth is better than oxygen annealed stacks.<sup>68,69</sup> Study reported that oxygen annealing atmosphere is responsible to decrease the concentration of oxygen vacancies.<sup>70</sup> Fig. 10(c) shows the schematic diagram of nitrogen annealed stack, the optimum

oxygen vacancies concentration was obtained due to generation of more oxygen vacancies, which caused further reduction of forming voltage and suppression of random filament formation. The nitrogen annealed stack exhibited that the endurance performance remains stable up to 800 switching cycles without degradation, which should be ascribed to generation of more oxygen vacancies and formation of confined CFs. The confined filament formation might be due to the increase of filament sizes. Zhou *et al.* theoretically investigated the influence of nitrogen annealing on the resistive switching characteristics based on Ti-doped  $\text{HfO}_2$  model using the first-principles calculation method, and confirmed that nitrogen annealing would cause a low oxygen vacancies formation energy and create more oxygen.<sup>70</sup> Ismail *et al.* reported that creating more oxygen vacancies can increase the size of CFs.<sup>71</sup> Yan *et al.* demonstrated the roles of oxygen vacancies and grain boundaries in  $\text{Ba}_{0.6}\text{Sr}_{0.4}\text{TiO}_3$  resistive switching films.<sup>11</sup> Their research suggested that grain boundaries serve as an oxygen reservoirs for accumulating the oxygen vacancies, associating with enlarging the size of grain boundaries due to generation of more oxygen vacancies.

## 4. Conclusions

Effect of annealing atmosphere (oxygen, air, and nitrogen) on resistive switching and magnetic properties of  $\text{Pt}/\text{Co}_3\text{O}_4/\text{Pt}$  stacks were investigated. Improvement in stability and uniformity of bipolar RS parameters was achieved at nitrogen annealed  $\text{Pt}/\text{Co}_3\text{O}_4/\text{Pt}$  stack due to the formation of confined CFs and suppressing the randomness of oxygen vacancies. The carrier transportation in LRS and the low voltage region of HRS is dominated by ohmic conduction, while the domination conduction is Schottky emission in the higher-voltage of HRS. Physical mechanism of RS was involved in formation and rupture of oxygen vacancies based CFs related to current-induced thermal effect. In addition, multilevel saturation magnetization was observed at different resistance states. The variation in saturation magnetization associated with RS is attributed to the oxygen vacancy concentration accompanying with the changes in the valence states of cations ( $\text{Co}^{2+}$  and  $\text{Co}^{3+}$ ). The nitrogen annealed  $\text{Pt}/\text{Co}_3\text{O}_4/\text{Pt}$  stack exhibited low electroforming voltage, excellent endurance, uniform set and reset voltage as well as good data retention. The achieved characteristics of the resistive switching in  $\text{Co}_3\text{O}_4$  films demonstrate a promising candidate for resistive random access memory applications.

## Conflicts of interest

The authors declare no conflict of interest.

## Acknowledgements

The authors gratefully acknowledge financial support from National Natural Science Foundation of China (No. 51872335, 51372281) and Natural Science Foundation of Guangdong Province, China (No. 2015A030311019).



## References

- 1 R. Waser, R. Dittmann, G. Staikov and K. Szot, *Adv. Mater.*, 2009, **21**, 2632–2663.
- 2 J. J. Yang, D. B. Strukov and D. R. Stewart, *Nat. Nanotechnol.*, 2013, **8**, 13–24.
- 3 W. Hu, N. Qin, G. H. Wu, Y. T. Lin, S. W. Li and D. H. Bao, *J. Am. Chem. Soc.*, 2012, **134**, 14658–14661.
- 4 X. M. Chen, W. Hu, Y. Li, S. X. Wu and D. H. Bao, *Appl. Phys. Lett.*, 2016, **108**, 053504.
- 5 M. Q. Guo, Y. C. Chen, C. Y. Lin, Y. F. Chang, B. Fowler, Q. Q. Li, J. Lee and Y. G. Zhao, *Appl. Phys. Lett.*, 2017, **110**, 233504.
- 6 Y. Li, K. S. Yin, M. Y. Zhang, L. Cheng, K. Lu, S. B. Long, Y. X. Zhou, Z. Wang, K. H. Xue, M. Liu and X. S. Miao, *Appl. Phys. Lett.*, 2017, **111**, 213505.
- 7 C. H. Huang, J. S. Huang, C. C. Lai, H. W. Huang, S. J. Lin and Y. L. Chueh, *ACS Appl. Mater. Interfaces*, 2013, **5**, 6017–6023.
- 8 N. Sedghi, H. Li, I. F. Brunell, K. Dawson, Y. Guo, R. J. Potter, J. T. Gibbon, V. R. Dhanak, W. D. Zhang, J. F. Zhang, S. Hall, J. Robertson and P. R. Chalker, *Appl. Phys. Lett.*, 2017, **111**, 092904.
- 9 M. Zhao, Y. D. Zhu, Y. Zhang, T. T. Zhang, D. Qiu, G. H. Lai, C. Hu, Q. W. Wang, F. Zhang and M. Y. Li, *RSC Adv.*, 2017, **7**, 23287–23292.
- 10 F. Z. Lv, C. X. Gao, P. Zhang, C. H. Dong, C. Zhang and D. S. Xue, *RSC Adv.*, 2015, **5**, 40714–40718.
- 11 X. B. Yan, Y. C. Li, J. H. Zhao, Y. Li, G. Bai and S. Q. Zhu, *Appl. Phys. Lett.*, 2016, **108**, 033108.
- 12 R. H. Yue, X. W. Sun, L. Wei, Y. F. Yin, J. T. Yin and W. F. Zhang, *J. Appl. Phys.*, 2014, **115**, 164501.
- 13 J. Jeon, J. Jung and K. H. Chow, *Appl. Phys. Lett.*, 2017, **111**, 242401.
- 14 G. Chen, C. Song, C. Chen, S. Gao, F. Zeng and F. Pan, *Adv. Mater.*, 2012, **24**, 3515–3520.
- 15 T. T. Guo, T. T. Tan and Z. T. Liu, *Appl. Surf. Sci.*, 2015, **351**, 704–708.
- 16 T. T. Tan, T. T. Guo and Z. T. Liu, *J. Alloys Compd.*, 2014, **610**, 388–391.
- 17 A. Z. Hao, M. Ismail, S. He, N. Qin, W. H. Huang, J. Wu and D. H. Bao, *RSC Adv.*, 2017, **7**, 46665–46677.
- 18 J. H. Yoon, J. H. Han, J. S. Jung, W. Jeon, G. H. Kim, S. J. Song, J. Y. Seok, K. J. Yoon, M. H. Lee and C. S. Hwang, *Adv. Mater.*, 2013, **25**, 1987–1992.
- 19 Q. Liu, S. B. Long, H. B. Lv, W. Wang, J. B. Niu, Z. L. Huo, J. N. Chen and M. Liu, *ACS Nano*, 2010, **4**, 6162–6168.
- 20 M. Akbari, M. Kim, D. Kim and J. Lee, *RSC Adv.*, 2017, **7**, 16704–16708.
- 21 J. C. Li, H. P. Cui and X. Y. Hou, *J. Alloys Compd.*, 2018, **752**, 247–252.
- 22 Z. W. Yue, G. Q. Tan, H. J. Ren, A. Xia, D. Shao, M. Y. Guo, W. Yang and Z. J. Chai, *ACS Appl. Mater. Interfaces*, 2017, **9**, 20205–20212.
- 23 Y. H. Sun, X. Q. Yan, X. Zheng, Y. C. Liu, Y. G. Zhao, Y. W. Shen, Q. L. Liao and Y. Zhang, *ACS Appl. Mater. Interfaces*, 2015, **7**, 7382–7388.
- 24 S. Rehman, J. H. Hur and D. K. Kim, *J. Phys. Chem. C*, 2018, **122**, 11076–11085.
- 25 D. S. Shang, L. Shi, J. R. Sun, B. G. Shen, F. Zhuge, R. W. Li and Y. G. Zhao, *Appl. Phys. Lett.*, 2010, **96**, 072103.
- 26 R. Dong, W. F. Xiang, D. S. Lee, S. J. Oh, D. J. Seong, S. H. Heo, H. J. Choi, M. J. Kwon, M. Chang, M. Jo, M. Hasan and H. Hwang, *Appl. Phys. Lett.*, 2007, **90**, 182118.
- 27 T. F. Deng, C. Ye, J. J. Wu, P. He and H. Wang, *Microelectron. Reliab.*, 2016, **57**, 34–38.
- 28 Y. Ahn and J. Y. Son, *Mater. Res. Bull.*, 2017, **85**, 255–258.
- 29 J. D. Jin, J. W. Zhang, R. E. Kemel, Y. Luo, P. Bao, M. Althobaiti, D. Hesp, V. R. Dhanak, Z. L. Zheng, I. Z. Mitrovic, S. Hall and A. M. Song, *J. Alloys Compd.*, 2016, **673**, 54–59.
- 30 X. M. Chen, G. H. Wu, P. Jiang, W. F. Liu and D. H. Bao, *Appl. Phys. Lett.*, 2009, **94**, 033501.
- 31 W. Hu, X. M. Chen, G. H. Wu, Y. T. Lin, N. Qin and D. H. Bao, *Appl. Phys. Lett.*, 2012, **101**, 063501.
- 32 W. Hu, L. L. Zou, R. Q. Chen, W. Xie, X. M. Chen, N. Qin and D. H. Bao, *Appl. Phys. Lett.*, 2014, **104**, 143502.
- 33 J. M. Li, X. L. Zeng and Z. A. Xu, *Appl. Phys. Lett.*, 2013, **103**, 232410.
- 34 W. Hu, L. L. Zou, X. G. Lin, C. Gao, Y. C. Guo and D. H. Bao, *Mater. Des.*, 2016, **103**, 230–235.
- 35 G. A. Babu, G. Ravi, T. Mahalingam, M. Navaneethan, M. Arivanandhan and Y. Hayakawa, *J. Phys. Chem. C*, 2014, **118**, 23335–23348.
- 36 X. M. Dang, X. F. Zhang, X. L. Dong, W. Q. Ruan, H. C. Ma and M. Xue, *RSC Adv.*, 2014, **4**, 54655–54661.
- 37 Y. J. Kwon, H. G. Na, S. Y. Kang, M. S. Choi, J. H. Bang, T. W. Kim, A. Mirzaei and H. W. Kim, *Sens. Actuators, B*, 2017, **239**, 180–192.
- 38 D. H. Chen, L. L. Peng, Y. F. Yuan, Y. Zhu, Z. W. Fang, C. S. Yan, G. Chen, R. Shahbazian-Yassar, J. Lu, K. Amine and G. H. Yu, *Nano Lett.*, 2017, **17**, 3907–3913.
- 39 Q. Q. Xiong, H. Y. Qin, H. Z. Chi and Z. G. Ji, *J. Alloys Compd.*, 2016, **685**, 15–21.
- 40 A. N. Naveen and S. Selladurai, *Electrochim. Acta*, 2014, **125**, 404–414.
- 41 H. Pang, X. R. Li, Q. X. Zhao, H. G. Xue, W. Y. Lai, Z. Hu and W. Huang, *Nano Energy*, 2017, **35**, 138–145.
- 42 G. L. Zhu, R. X. Ge, F. L. Qu, G. Du, A. M. Asiri, Y. D. Yao and X. P. Sun, *J. Mater. Chem. A*, 2017, **5**, 6388–6392.
- 43 S. Farhadi, K. Pourzare and S. Bazgir, *J. Alloys Compd.*, 2014, **587**, 632–637.
- 44 L. Chen, F. C. Hu, H. L. Duan, Q. H. Liu, H. Tan, W. S. Yan, T. Yao, Y. Jiang, Z. H. Sun and S. Q. Wei, *Appl. Phys. Lett.*, 2016, **108**, 252402.
- 45 Y. Q. Xiong, W. P. Zhou, Q. Li, M. C. He, J. Du, Q. Q. Cao, D. H. Wang and Y. W. Du, *Appl. Phys. Lett.*, 2014, **105**, 032410.
- 46 Q. W. Wang, Y. D. Zhu, X. L. Liu, M. Zhao, M. C. Wei, F. Zhang, Y. Zhang, B. L. Sun and M. Y. Li, *Appl. Phys. Lett.*, 2015, **107**, 063502.
- 47 A. Z. Hao, M. Ismail, S. He, N. Qin, R. Q. Chen, A. M. Rana and D. H. Bao, *Mater. Sci. Eng., B*, 2018, **229**, 86–95.



- 48 G. Y. Chen, G. F. Bi, L. Song, Y. K. Weng, D. F. Pan, Y. C. Li, S. Dong, T. Tang, J. M. Liu and J. G. Wan, *Appl. Phys. Lett.*, 2016, **109**, 112903.
- 49 J. M. Li, *ACS Appl. Mater. Interfaces*, 2017, **9**, 39626–39634.
- 50 Q. Q. Gao, Q. X. Yu, K. Yuan, X. N. Fu, B. Chen, C. X. Zhu and H. Zhu, *Appl. Surf. Sci.*, 2013, **264**, 7–10.
- 51 J. M. Li and X. L. Zeng, *Appl. Phys. Lett.*, 2017, **110**, 083107.
- 52 J. M. Li, A. C. H. Huan, L. Wang, Y. W. Du and D. Feng, *Phys. Rev. B: Condens. Matter Mater. Phys.*, 2000, **61**, 6876–6878.
- 53 H. C. Wan, Y. G. Liu, H. Z. Zhang, W. X. Zhang, N. Jiang, Z. Y. Wang, S. H. Luo, H. Arandiyana, H. Liu and H. Y. Sun, *Electrochim. Acta*, 2018, **281**, 31–38.
- 54 M. Ismail, A. Z. Hao, W. H. Huang, J. J. Lee, S. J. Kim and D. H. Bao, *Appl. Phys. Lett.*, 2018, **113**, 152103.
- 55 K. Usha, P. Kumbhakar and B. Mondal, *Mater. Sci. Semicond. Process.*, 2016, **43**, 17–24.
- 56 S. J. Wang, B. P. Zhang, C. H. Zhao, S. J. Li, M. X. Zhang and L. P. Yan, *Appl. Surf. Sci.*, 2011, **257**, 3358–3362.
- 57 J. X. Hao, S. L. Peng, H. Q. Li, S. Dang, T. F. Qin, Y. X. Wen, J. J. Huang, F. Ma, D. Q. Gao, F. Li and G. Z. Cao, *J. Mater. Chem. A*, 2018, **6**, 16094–16100.
- 58 Y. Lchiyangi and S. Yamada, *Polyhedron*, 2005, **24**, 2813–2816.
- 59 M. Venkatesan, C. B. Fitzgerald and J. M. D. Coey, *Nature*, 2004, **430**, 630.
- 60 M. Zhao, Y. D. Zhu, M. Y. Li, Y. Zhang, X. Y. Tan, C. Hu, Q. W. Wang, F. Zhang, S. Z. Pu and R. Xiong, *J. Phys. D: Appl. Phys.*, 2017, **50**, 265102.
- 61 J. Chen, X. F. Wu and A. Selloni, *Phys. Rev. B: Condens. Matter Mater. Phys.*, 2011, **83**, 245204.
- 62 L. M. Apátiga and V. M. Castaño, *Thin Solid Films*, 2006, **496**, 576–579.
- 63 S. Farhadi and J. Safabakhsh, *J. Alloys Compd.*, 2012, **515**, 180–185.
- 64 S. Q. Ren, H. W. Qin, J. P. Bu, G. C. Zhu, J. H. Xie and J. F. Hu, *Appl. Phys. Lett.*, 2015, **107**, 062404.
- 65 M. Zhao, Y. D. Zhu, Q. G. Wang, M. C. Wei, X. L. Liu, F. Zhang, C. Hu, T. T. Zhang, D. Qiu, M. Y. Li and R. Xiong, *Appl. Phys. Lett.*, 2016, **109**, 013504.
- 66 X. Gao, H. X. Guo, Y. D. Xia, J. Yin and Z. G. Liu, *Thin Solid Films*, 2010, **519**, 450–452.
- 67 A. Younis, D. Chu, X. Lin, J. Lee and S. Li, *Nanoscale Res. Lett.*, 2013, **8**, 36.
- 68 A. Z. Hao, M. Ismail, S. He, N. Qin, W. H. Huang, J. Wu and D. H. Bao, *J. Alloys Compd.*, 2018, **732**, 573–584.
- 69 L. G. Wang, Z. Y. Cao, X. Qian, L. Zhu, D. P. Cui, A. D. Li and D. Wu, *ACS Appl. Mater. Interfaces*, 2017, **9**, 6634–6643.
- 70 H. Zhou, X. D. Wei, W. Wei, C. Ye, R. L. Zhang, L. Zhang, Q. Xia, H. Huang and B. Wang, *Surf. Coat. Technol.*, 2019, **359**, 150–154.
- 71 M. Ismail, E. Ahmed, A. M. Rana, F. Hussain, L. Talib, M. Y. Nadeem, D. Panda and N. A. Shah, *ACS Appl. Mater. Interfaces*, 2016, **8**, 6127–6136.

